

Temperature Promotes Selectivity During Electrochemical CO₂ Reduction on NiO:SnO₂ Nanofibers

M. A. Rodriguez-Olguin,[#] R. Lipin,[#] M. Suominen, F. Ruiz-Zepeda, E. Castañeda-Morales, A. Manzo-Robledo, J.G.E. Gardeniers, C. Flox,^{*} T. Kallio,^{*} M. Vandichel,^{*} A. Susarrey-Arce^{*}

[#]These authors contributed equally to this work

^{*}Corresponding author(s): cristina.flox@ciiae.org; tanja.kallio@aalto.fi; matthias.vandichel@ul.ie;
a.susarreyarce@utwente.nl

1. Ni- and NiO electrocatalysts

Table S1. Ni/NiO electrocatalyst used for formate and other products during CO₂RR.

Compound	Synthesis Method	Main product	Electrolyte	FE	E (vs RHE)	J _{lucoc-} (mA/cm ²)	T (°C)	Reference
NiO@Cl-9%	Electrospinning	HCOO ⁻	0.1M KHCO ₃	70%	-0.8 V	14.7	25	¹
Ni-N-C	In situ carbonization	CO	0.1 M KHCO ₃	90%	-0.8V	5.0 (for CO)	25	²
Ni atomic/carbon	Pyrolysis	CO	0.5 M KHCO ₃	90%	-1.0 V	57.1 (for CO)	25	³
Ni single atoms/CNF	Electrospinning	CO	0.5M KHCO ₃	88%	-1.0 V	308.4 (for CO)	25	⁴
Ni/NiO/g-C₃N₄	Photocatalytic reduction	CO	0.5 M Na ₂ SO ₄	87%	-0.3 V	7.8 μA/cm ²	25	⁵
NiO doped Zn²⁺	Combustion synthesis	C ₂ H ₄	0.5 M NaHCO ₃	47%	-0.79 V	N.R.	25	⁶
Ni-N₃	Impregnation, ZIF formation	CO	0.5 M KHCO ₃	95%	-1.0 V	27	25	⁷
Ni-N doped CNT	CVD	CO	0.5 KHCO ₃	91%	-0.74 V	29	25	⁸
Ni single atoms-N-C	Ball-milling, pyrolysis	CO	0.1 KHCO ₃	93%	-1.3 V	16.5	25	⁹
Ni-N_{4-x}-C_x	Pyrolysis	CO	Humidified CO ₂	99%	-2.0 V	470	25	¹⁰
Co-N-Ni	Sonochemistry	CO	0.1 M KHCO ₃	94.6%	- 370 mV	1.7	25	¹¹
Ni/Ni₃ZnC_{0.7}-NC	Hydrothermal	CO	0.5 KHCO ₃	92.5%	- 0.87 V	15.77	25	¹²
NiN_x/NCNT	Ball-milling, annealing	CO	1 M KOH	99%	-0.272 V	85.6	25	¹³
Ni-N₄ in mesoporous carbon	Solvent drying and annealing	CO	0.5 KHCO ₃	95%	-0.8 V	366	25	¹⁴
Ni single atom/Ni NP/MOF	Pyrolysis	CO	1 M KOH	99%	-1.82 V	160	25	¹⁵
CuZn-Ni aerogel	Aerogel synthesis	CO	1M KOH	80%	-0.8 V	20.0	25	¹⁶
Ni-SAC-nano array	Hydrothermal, annealing	CO	0.5 KHCO ₃	90%	-1.0 V	66.0	25	¹⁷

2. Sn and SnO₂ electrocatalysts

Table S2. Sn/SnO₂ electrocatalyst for formate formation during CO₂RR.

Compound	Synthesis Method	Main product	Electrolyte	FE	E (vs RHE)	J _{HCOO-} (mA/cm ²)	T (°C)	Reference
SnO₂-Cl doped	Sonochemistry	HCOO ⁻	2M KHCO ₃	59.1%	1.3	32.6	25	¹⁸
Anodic SnO₂	Anodic oxidation	HCOO ⁻	0.5M KHCO ₃	73%	0.8	10	25	¹⁹
Mn-doped atomic SnO₂ layers	Hydrothermal	HCOO ⁻	0.1M KHCO ₃	75%	1.03	21.2	25	²⁰
Zn-Sn oxides	Biomineralization	HCOO ⁻	0.1M KHCO ₃	70%	-1.1 V	8.4 (for CO + HCOOH)	25	²¹
SnO₂/C	Impregnation	HCOO ⁻	0.5 M KHCO ₃	92%	0.86 V	29	25	²²
Sn-halogen incorporated	Hydrolysis	HCOO ⁻	0.5 M KHCO ₃	96%	-0.9 V	62.4	25	²³
SnO nanosheets	Precipitation	HCOO ⁻	1M KOH	94%	0.7V	330	25	²⁴
SnO₂/GO	Hydrothermal	HCOO ⁻	0.1M KHCO ₃	84.4%	0.96V	4.5	25	²⁵
VO-rich N-SnO₂	Hydrothermal	HCOO ⁻	0.1M KHCO ₃	83%	0.9V	10	25	²⁶
Ov-engineered SnO₂	Thermal treatment	HCOO ⁻	1 M KHCO ₃	80%	-0.9 V	16.6	25	²⁷
B-doped SnO₂	Hydrothermal	HCOO ⁻	0.5M KHCO ₃	95%	1.0 V	43.2	25	²⁸
SnO₂ nanosheets	Solvothermal	HCOO ⁻	0.1M NaHCO ₃	83%	320 mV	16	25	²⁹
SnO₂/OC	Hydrothermal	HCOO ⁻	0.1M KHCO ₃	75%	1.29 V	13.4	25	³⁰
SnO_x	Deposition	HCOO ⁻	0.5M KHCO ₃	69%	1.0	53	25	³¹
Wavy SnO₂	Hydrothermal	HCOO ⁻	0.5M KHCO ₃	22%	1.0 V	87	25	³²
Porous SnO₂ nanosheets	CVD	HCOO ⁻	0.5M KHCO ₃	94%	0.51 V	18.8	25	³³
Chainlike Mesoporous SnO₂	Anodic oxidation	HCOO ⁻	0.1M KHCO ₃	82%	1.06 V	15.3	25	³⁴
SnO₂-GQDs	Hydrothermal	HCOO ⁻	0.1M KHCO ₃	93%	1.3V	16.2	25	³⁵
SnO_x Nanosheets-MWCNTs	Hydrothermal	HCOO ⁻	0.5M KHCO ₃	77%	1.25V (vs SHE)	11.0	25	³⁶
Double-shell SnO_x nanosphere	Hydrothermal	HCOO ⁻	0.5M KHCO ₃	81%	1.15 V	44.7	25	³⁷
1D SnO₂	Electrospinning	HCOO ⁻	0.1M KHCO ₃	70%	1.29 V	12.0	25	³⁸
Sn/SnO₂ nanofiber	Electrospinning	HCOO ⁻	0.1M KHCO ₃	82.1%	1.6 V (vs SCE)	22.9	25	³⁹

3. Ni:Sn metal or metal oxide electrocatalysts

Table S3. Ni:Sn metal or metal oxide electrocatalyst used for formate formation during CO₂RR.

Compound	Synthesis Method	Main product	Electrolyte	FE	E (vs RHE)	J _{HCOO-} (mA/cm ²)	T (°C)	Reference
N₄-Ni-Sn-N₄ SAC	Impregnation	HCOOH	0.5 M KHCO ₃	86.1%	-0.82 V	43.7	25	⁴⁰
Ni-doped SnO₂	Solvothermal	HCOOH	1 M KOH	80%	-1.2 V	116	25	⁴¹

4. SnO₂-based model

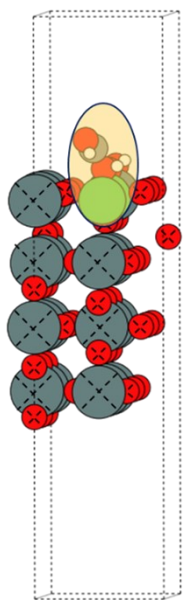


Figure S1. An ASE-GUI representation of the model system for the vibrational analysis. The constrained atoms are marked with a dashed X, and the unfixed atoms are highlighted in yellow.⁴²

Table S4. Thermodynamic quantities for the gas phase molecules in eV.

	E _{DFT}	ZPE	$\int_0^{298} C_v dT$	TS	G
H ₂	-6.7619	0.27	0.09	0.43	-6.832
H ₂ O	-14.2336	0.56	0.10	0.67	-14.24
CO ₂	-23.0229	0.31	0.10	0.66	-23.273
HCOOH	-29.8814	0.89	0.11	1.05	-29.93

5. Morphological inspection for NiO, SnO₂, and NiOSnO25NF

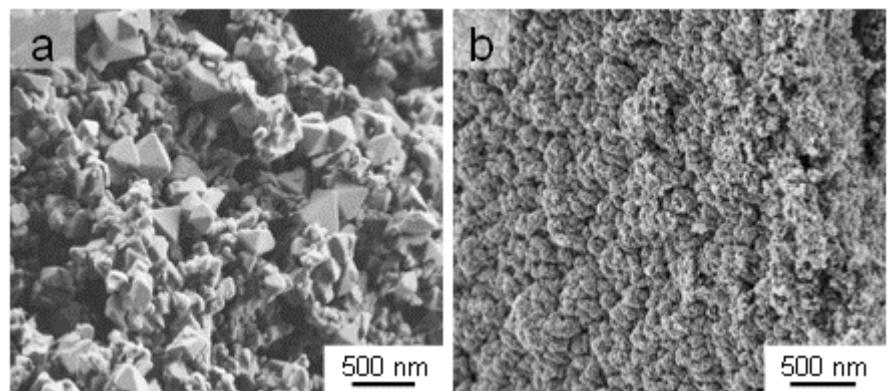


Figure S2. SEM image of (a) NiO and (b) SnO₂.

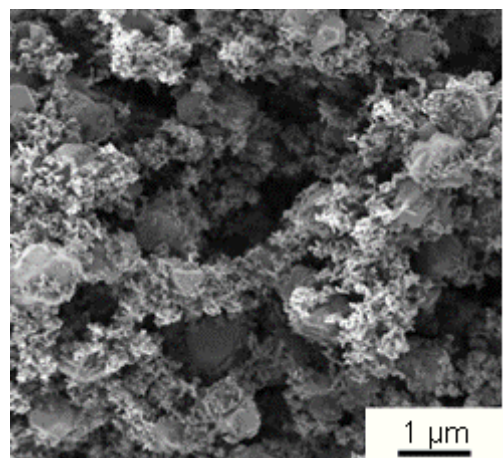


Figure S3. SEM image of NiOSnO25NF.

6. Interface structure between NiO and SnO₂ nanocrystals

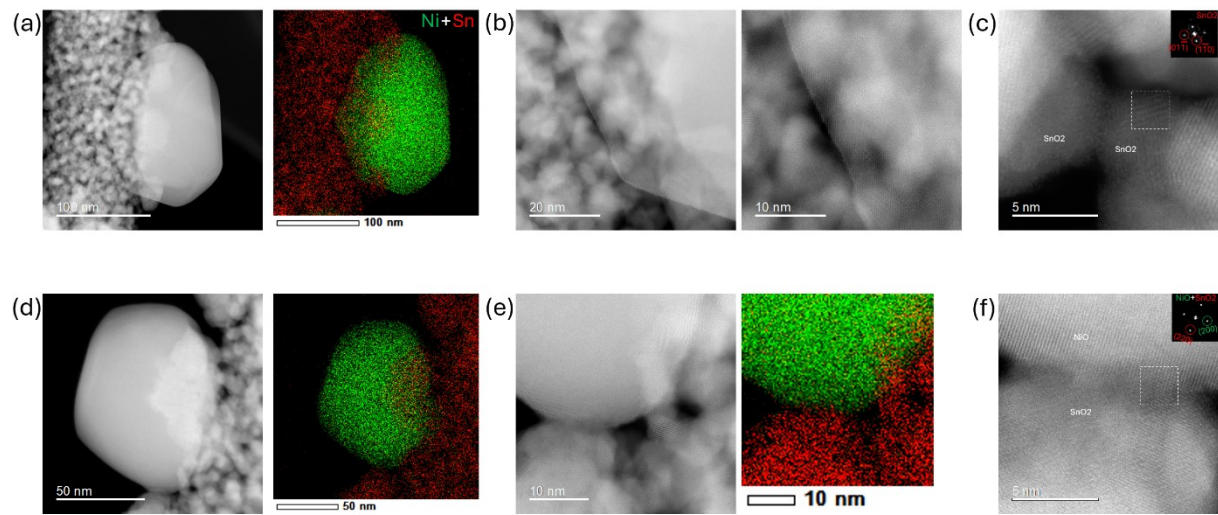


Figure S4. Interface structure between NiO and SnO₂ nanocrystallites. (a) ADF and EDX map of the NiO crystallite decorating a nanofiber. (b) Close-up of a NiO crystallite edge laying on the nanofiber with multiple SnO₂ nanocrystallites homogeneously assembled. (c) An interface between two SnO₂ nanocrystallites shows that the contact planes for one of the nanocrystallites observed along the zone axis [111] correspond to 011. (d) ADF and EDX map of a second example of a NiO crystallite sitting on the nanofiber. (e) A close-up ADF and EDX map showing the interaction on multiple contact points of the large NiO crystallite with the SnO₂ nanocrystallites. (f) Interface between the NiO crystallite and SnO₂ nanocrystallites. The exposed facets of the observed SnO₂ nanocrystallites correspond to 220 planes, while the NiO crystallite facet in contact exhibits a surface with multiple steps that are oriented perpendicular to 200 planes. This illustrates that the NiO crystallite fits a non-sharp interface but is still aligned with the multigrain arrangement of the SnO₂ nanoparticles that construct the nanofiber.

7. Electrochemical impedance spectroscopy

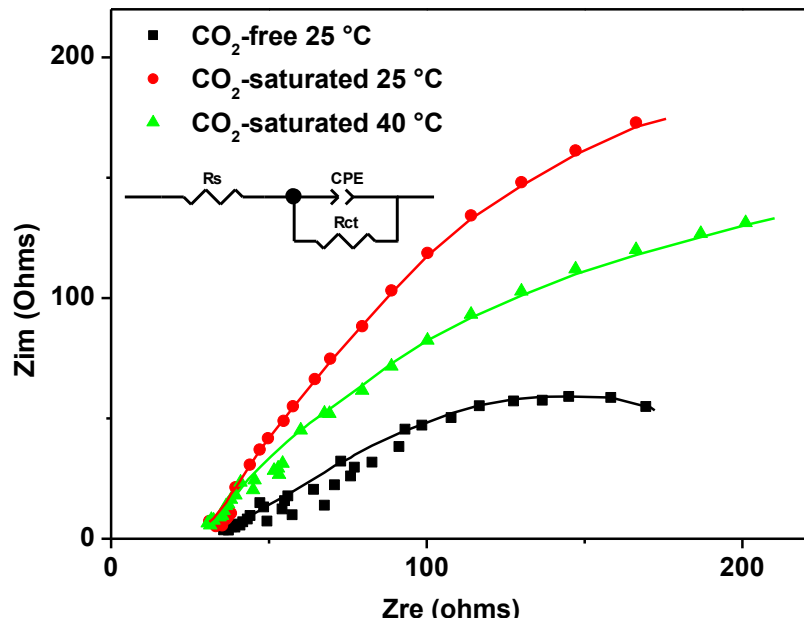


Figure S5. Nyquist plots for NiOSnO₇₅NF without and saturated with CO₂ at different temperatures in 0.1 M KHCO₃

Table S5. Electric parameters for NiOSnO₇₅NF over various temperatures. For the experimental results, see **Figure S5**.

Conditions	R_s	R_{ct}	CPE-P	CPE-T
CO ₂ -free (25 °C)	33.16	424.60	0.45191	0.00451
CO ₂ -saturated (25 °C)	31.12	764.51	0.65253	0.00291
CO ₂ -saturated (40 °C)	33.74	511.75	0.59552	0.00395

The R_{ct} values in **Table S5** indicate that NiOSnO₇₅NF has a higher affinity to CO₂. In the absence of CO₂, the affinity to H₂ might be preferred.

8. Linear scan voltammetry

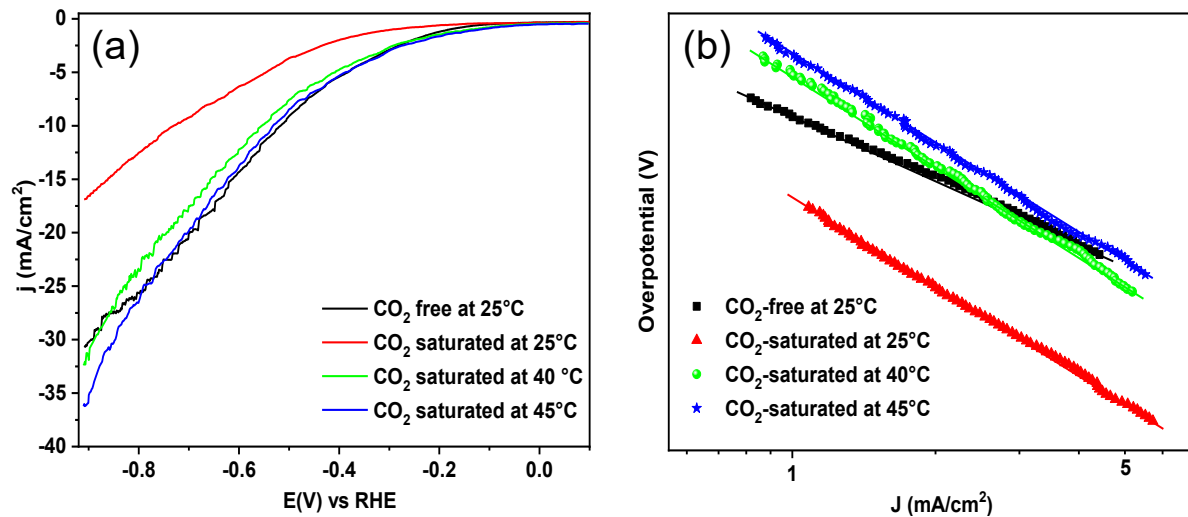


Figure S6. (a) Linear scan voltammetry (LSV) and (b) Tafel slopes derived from LSV in the absence and presence of CO_2 at 25 °C (black line/closed square circles and red line/closed triangles), 40 °C (green line/closed green circles), and 45°C (blue line/blue asterisks) for NiOSnO75NF in 0.1 M KHCO_3 .

Table S6. Tafel slopes for NiOSnO75NF over various temperatures. For the experimental results, see **Figure S6**.

Conditions	Tafel Slope (mV/dec)
CO_2 -free (25 °C)	210
CO_2 -saturated (25 °C)	302
CO_2 -saturated (40 °C)	293
CO_2 -saturated (45 °C)	278

9. Electrochemical measurements and HCOOH fragments

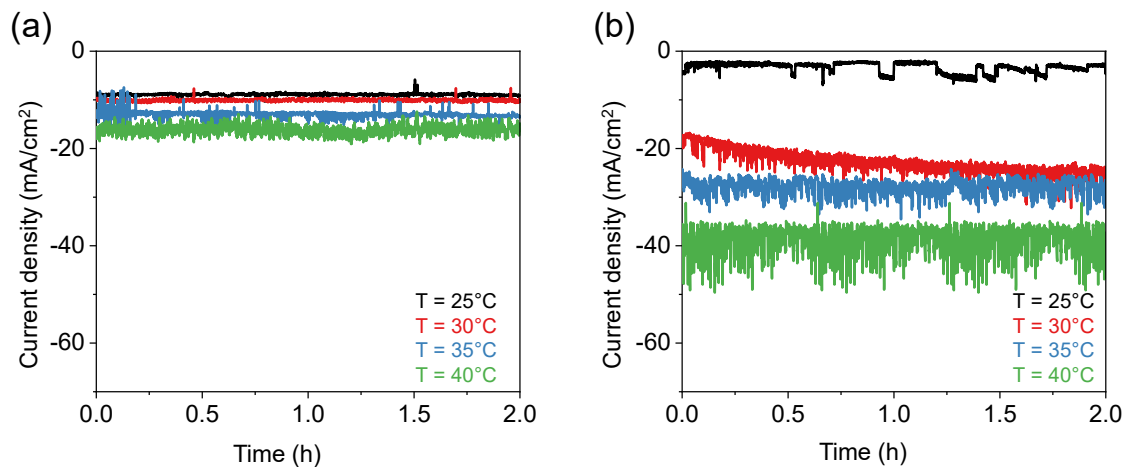


Figure S7. Chronoamperogram of NiOSn50NF and NiOSnO75NF in the presence of CO_2 over various temperatures and applied cell potentials of -0.85 vs. RHE.

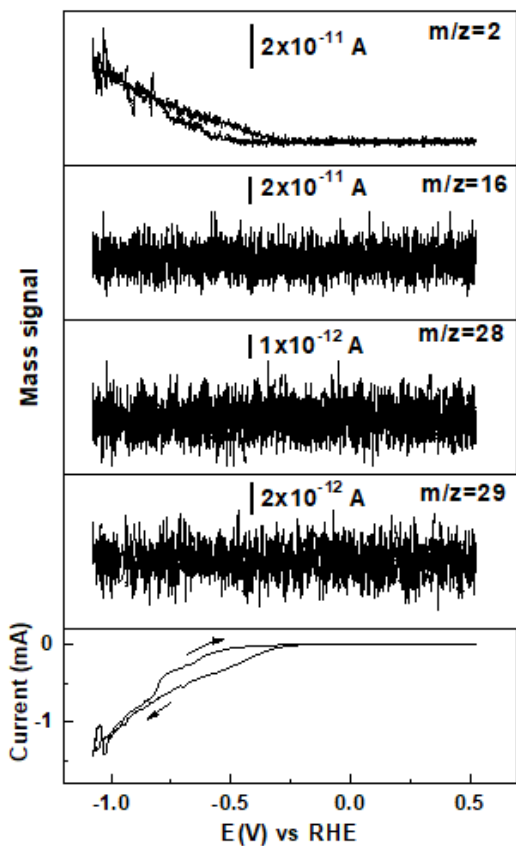


Figure S8. CV characteristic for NiOSnO75NF at 25°C in the absence of CO_2 . The mass signal is also shown as a function of the applied potential (1 mV/s) for $m/z = 2$, $m/z = 16$, $m/z = 28$, and $m/z = 29$.

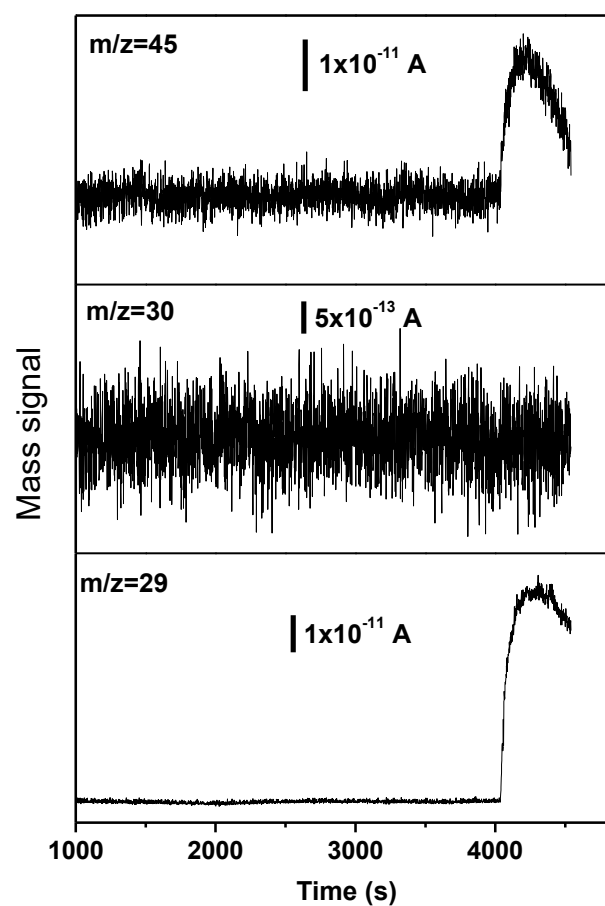


Figure S9. The mass signal of HCOOH for $m/z = 45$, $m/z = 30$, and $m/z = 29$ fragments.

10. Chemical characterization with STEM-EDX

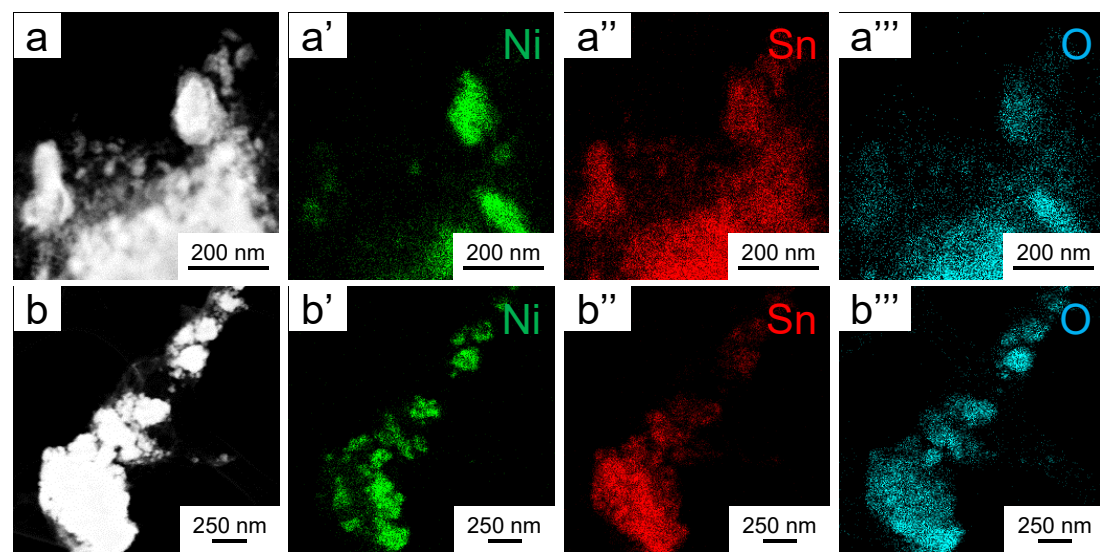


Figure S10. Representative STEM-ADF and STEM-EDX maps for NiOSnO₇₅NF after 2 h (a) and 22 h (b) of CO₂ electrolysis.

11. Raman

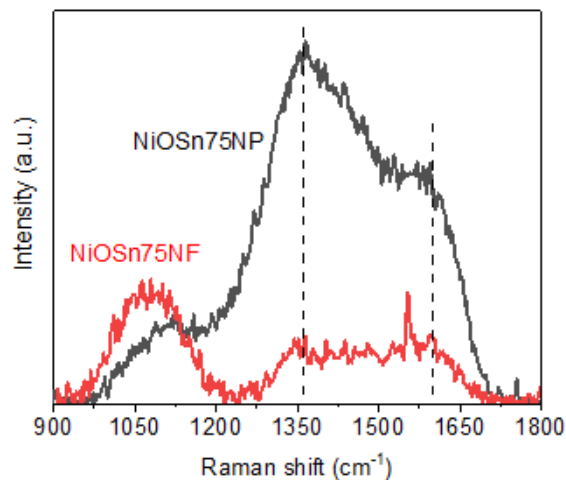


Figure S11. Representative Raman spectra for NiOSnO75NF and NiOSnO75NP

In **Figure S11**, the Raman spectrum is shown. The first peak at 1359 cm^{-1} is identified as a defective or disordered carbon lattice.⁴³ The peak at 1596 cm^{-1} correlates with graphitic carbon species.^{44,45} The results demonstrate that NiOSnO75NP retains more carbon remnants than NiOSnO75NF.

12. STEM-ADF micrographs for NiOSnO₇₅NF with and without surfactant

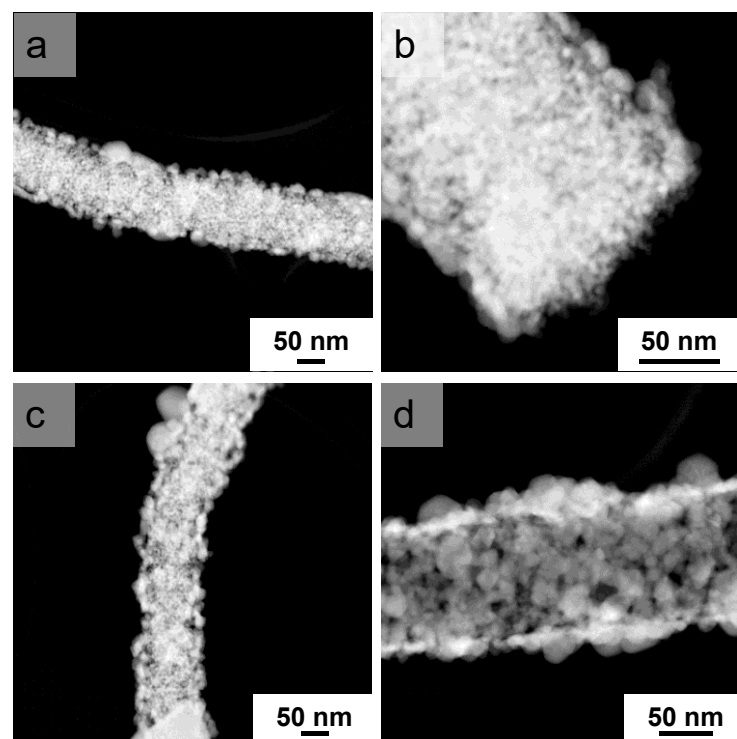


Figure S12. STEM-ADF micrographs of (a-b) NiOSnO₇₅NF and (c-d) NiOSnO₇₅ with surfactant.

13. CO₂RR for NiOSnO₇₅NF with surfactant

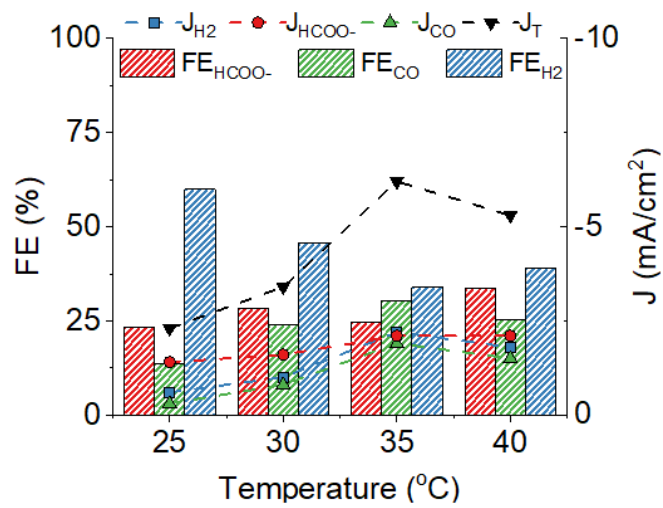


Figure S13. Product distribution for NiOSnO₇₅NF with surfactant at -0.85 vs. RHE for 2 h over various temperatures, i.e., 25, 30, 35, 40 °C.

14. Computational Insights

Cohesive Energy: Cohesive energy is considered a well-known descriptor to estimate the stability of surface slabs for bulk structures.⁴⁶ The relative stabilities of Ni-doped SnO₂ are examined from the SnO₂ and NiO bulk structures. The cohesive energy (E_{coh}) for an undoped SnO₂(hkl) slab can be expressed as follows:

$$E_{Coh} = \frac{E_{SnO_2(hkl)} - (N_{units}^{SnO_2} E_{bulk}^{SnO_2})}{(a+b)} \quad (1)$$

where $E_{SnO_2(hkl)}$, $E_{bulk}^{SnO_2}$ are the energies of a pristine SnO₂ slab and bulk SnO₂ in a tetragonal lattice, respectively. $N_{units}^{SnO_2}$, a and b are the number of SnO₂ per unit formula, Sn and O atoms, respectively. Furthermore, the cohesive energy for Ni-doped SnO₂ systems can be computationally determined:

$$E_{Coh} = \frac{E_{Ni@SnO_2(hkl)} - (N_{units}^{SnO_2} E_{bulk}^{SnO_2} + N_{units}^{NiO} E_{bulk}^{NiO}) + 0.5N_{O_2} E_{O_2}}{(a + b + c)} \quad (2)$$

where $E_{Ni@SnO_2(hkl)}$, is the total energy of the doped SnO₂ surface slab, and E_{bulk}^{NiO} , E_{O_2} are the energies of bulk NiO in a cubic lattice and O₂ gas molecule, respectively. The factors a, b, and c are the number of Sn, Ni, and O in the Ni-doped systems. The more negative the cohesive energy is compared to pure SnO₂, the more stable the doped phase.⁴⁷ The cohesive energy per atom increases in the order 2Ni@SnO₂ > Ni@SnO₂ > SnO₂ (**Table S7**). As the concentration of the Ni increases, the cohesive energy becomes more negative, implying the desirable formation of Ni-doped phases.

Surface Formation Energy: The surface formation energy (γ) is the energy needed to create a surface with (hkl) termination from its bulk and is often used as a descriptor for surface stability.^{48,49} Herein, model systems with a (110) termination of SnO₂ are studied because it is the most abundant surface in all experimental samples studied, as identified by experimental XRD data (**Figure 3**). A surface with low γ implies a stable surface. The surface formation energy for the (110) terminated SnO₂ is given as:

$$\gamma_{SnO_2(110)} = \frac{1}{2A} (E_{SnO_2} - N_{units}^{SnO_2} E_{bulk}^{SnO_2}) \quad (3)$$

Here, A represents the surface area multiplied with a factor 2 because of the assumption of symmetric terminations of the $\text{SnO}_2(110)$ model. Note that for the $\text{SnO}_2(110)$, there are several possible terminations, and herein, we considered the O-terminated surface as it has garnered significant interest in previous theoretical investigations.⁵⁰⁻⁵² However, in the case of Ni doping, the terminations will become asymmetric, and the surface formation energy of the Ni-doped side of the model system can then be defined as:

$$\gamma = \gamma_{\text{Ni@SnO}_2(110)} - \gamma_{\text{SnO}_2(110)} \quad (4)$$

where $\gamma_{\text{Ni@SnO}_2(110)}$ and $\gamma_{\text{SnO}_2(110)}$ are the surface formation energies of the Ni@SnO_2 and pristine SnO_2 model systems (in **Table S2** and **Figure S11-13**, γ or surface formation energy of the modified surface is displayed). $\gamma_{\text{Ni@SnO}_2(110)}$ is calculated as:

$$\gamma_{\text{Ni@SnO}_2(110)} = \frac{1}{A} (\text{E}_{\text{Ni@SnO}_2(110)} - (\text{N}_{\text{units}}^{\text{SnO}_2} \text{E}_{\text{bulk}}^{\text{SnO}_2} + \text{N}_{\text{units}}^{\text{NiO}} \text{E}_{\text{bulk}}^{\text{NiO}}) + 0.5 \text{N}_{\text{O}_2} \text{E}_{\text{O}_2}) \quad (5)$$

Table S7 shows the surface formation energies of Ni-doped and pristine SnO_2 systems. Like the cohesive energy, the surface energies of the Ni-doped system are low (and negative) compared to SnO_2 , representing a stable surface for the doped systems. Overall, the cohesive and surface energies from the bulk oxides and O_2 confirm the higher stability of the Ni-doped $\text{SnO}_2(110)$ phases over pristine $\text{SnO}_2(110)$ phases.

Table S7. Cohesive (in eV/atom) and surface formation energies (in eV/ \AA^2) of the slabs studied.

	E_{coh} (in eV/atom)	Surface Formation Energy (eV/ \AA^2)
$\text{SnO}_2(110)$	0.16	0.09
$\text{Ni@SnO}_2(110)$	0.06	-0.02
$2\text{Ni@SnO}_2(110)$	-0.04	-0.21

15. Computational Insights on NiO/SnO₂ Interface

The stability of the interface between the NiO and SnO₂ is investigated by constructing a large 3×2 supercell of the existing SnO₂(110) model with four SnO₂ layers as previously used. Due to the complexity of the large supercell models (~450 atoms), we performed non-spin polarized calculations with the Brillouin zone sampling restricted to the Γ -point, keeping all other parameters unchanged. The surface formation energy (SFE) of various Ni-containing surfaces on both pristine and reduced SnO₂ (SnO/SnO₂) are calculated using equation (4) and (5). It should be noted that the surface Pourbaix diagrams in **Figure 6** indicate that the surface tends to reduce under experimental conditions, making it crucial to consider reduced SnO₂ surface models when describing NiO/SnO₂ interfaces.

The different Ni-containing systems considered are: (1) Ni at adatom positions, (2) Ni doped at six-coordinated Sn surface positions (position 1), and (3) Ni doped at five-coordinated Sn surface positions (position 2). We have also constructed a NiO ($\text{Ni}_{32}\text{O}_{32}$) nanocube adsorbed and a system with all surface Sn atoms replaced by Ni atoms (NiO/SnO₂ and NiO₂/SnO₂).

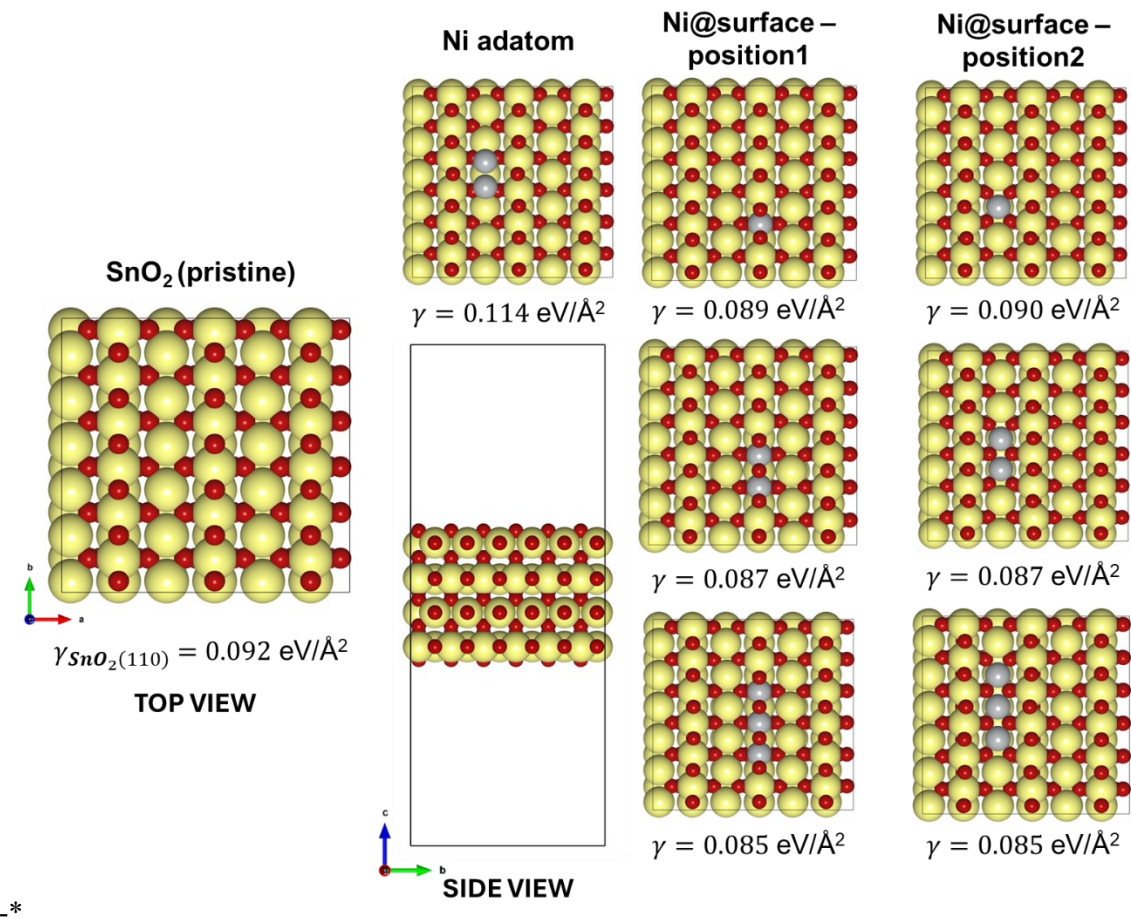


Figure S14. Optimized geometries of different Ni-containing systems over SnO₂ and their corresponding surface formation energies in eV/Å² calculated using Eq. 4. Color codes: Sn (yellow), O (red), and Ni (grey).

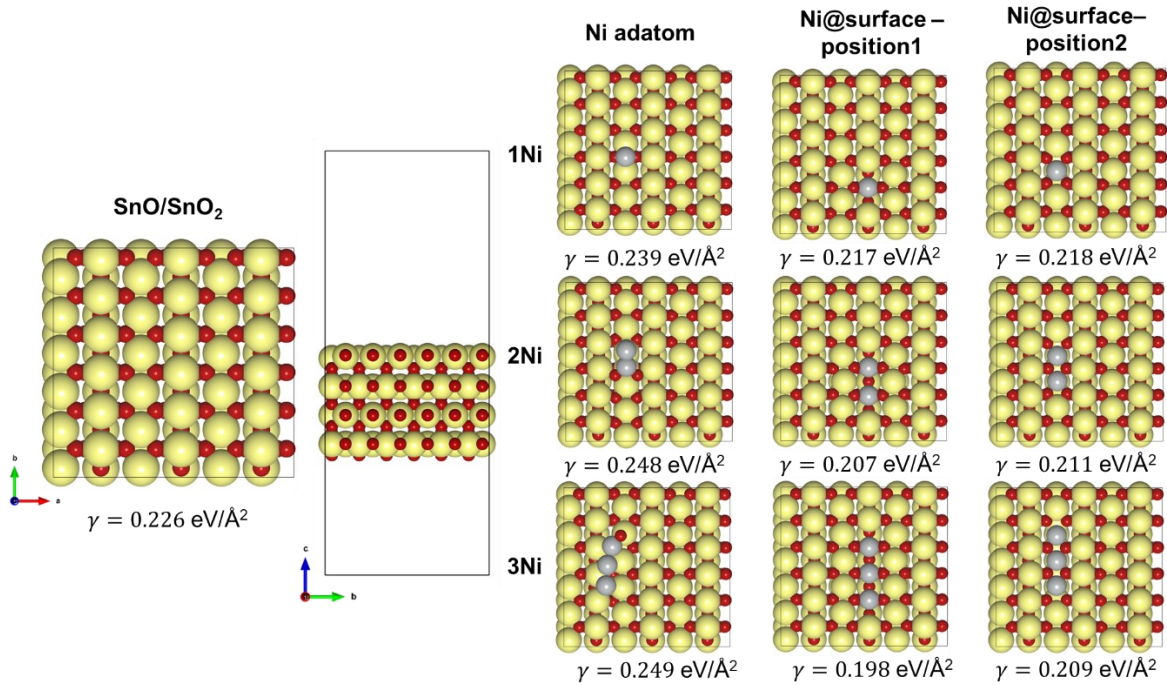


Figure S15. Optimized geometries of different Ni-containing systems over reduced SnO_2 (SnO/SnO_2) and their corresponding surface formation energies in $\text{eV}/\text{\AA}^2$ calculated using Eq. 4. Color codes: Sn (yellow), O (red), and Ni (grey).

From **Figure S14 and S15**, it is observed that Ni lowers the surface formation energy with respect to pristine SnO_2 , where the Ni atoms pull and compress the surrounding atoms from their lattice positions, similar to the small models discussed previously. The surface formation energy of 1.00 ML NiO overlayer on a reduced surface (NiO/SnO_2) was the lowest observed, with $-0.347 \text{ eV}/\text{\AA}^2$ compared to the various Ni-containing systems studied (**Figure S16**). The same configuration on the pristine SnO_2 ($\text{NiO}_2/\text{SnO}_2$) also exhibited a lower surface energy ($0.049 \text{ eV}/\text{\AA}^2$), the least among the Ni-containing systems with pristine SnO_2 . Overall, the formation energies are an indication of the plausibility for a NiO phase supported by SnO_2 under the electrochemical conditions, corroborating experimental observations (**Figure S4**).

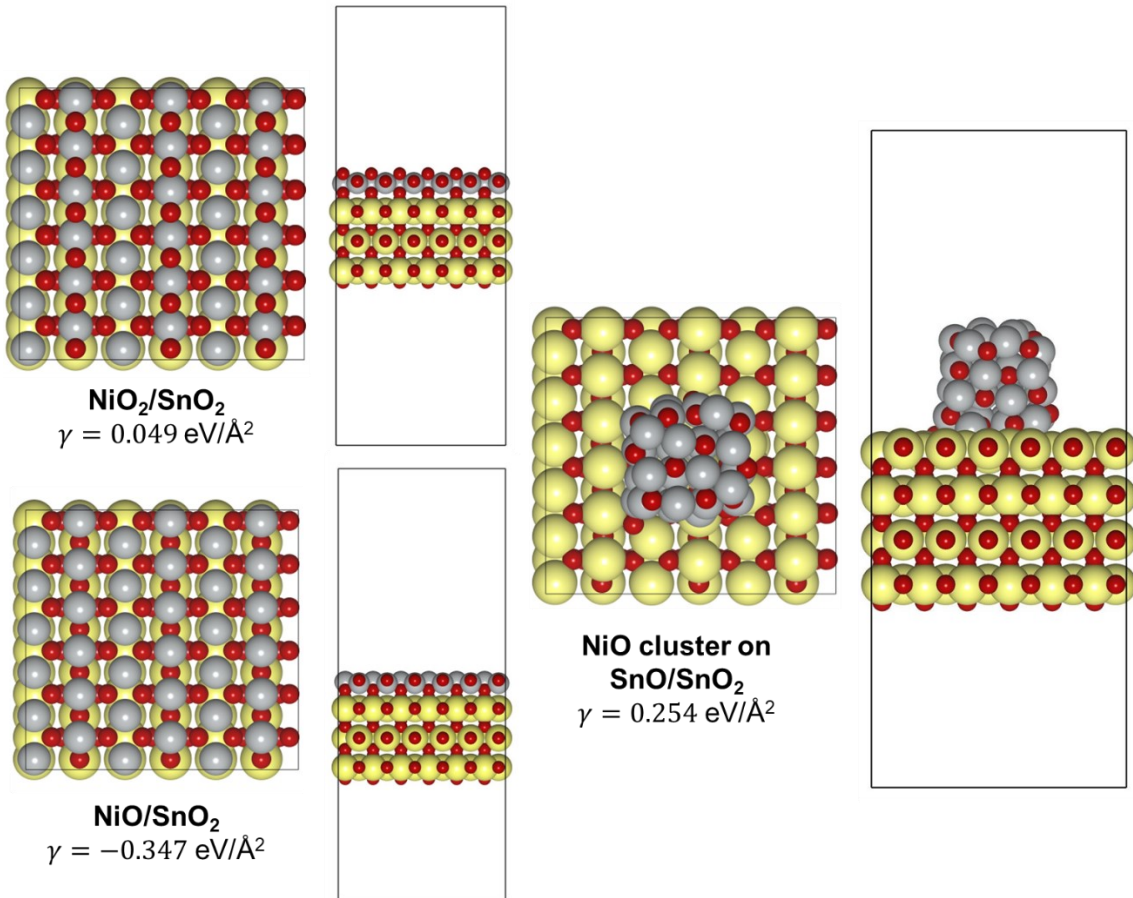


Figure S16. Optimized geometries of different NiO systems over pristine and reduced SnO₂ (SnO/SnO₂) models and their corresponding surface formation energies in eV/Å² calculated using Eq. 4. Color codes: Sn (yellow), O (red), and Ni (grey).

16. Gibbs Free Energy Vs Potential (pH=0)

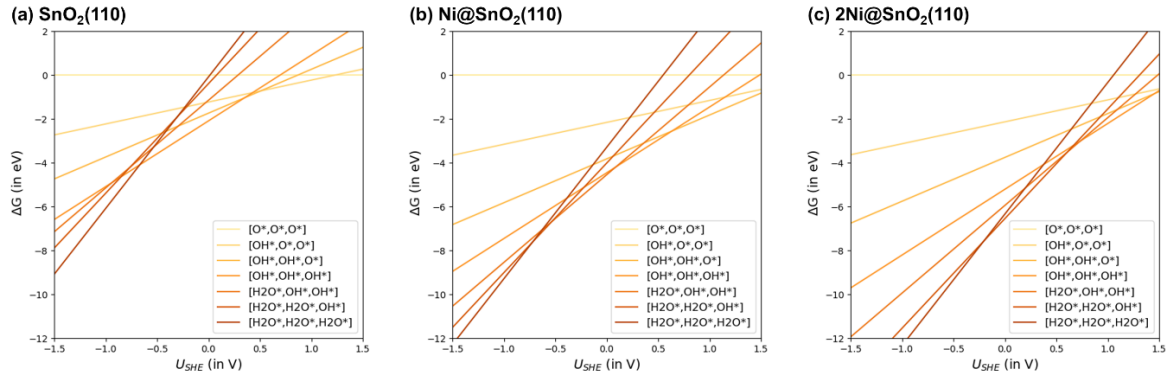


Figure S17. Gibbs free energy profiles as a function of U_{SHE} diagrams at $\text{pH} = 0$ for the studied $\text{SnO}_2(110)$ models.

References

- 1 M. A. Rodriguez-Olguin, C. Flox, R. Ponce-Pérez, R. Lipin, F. Ruiz-Zepeda, J. P. Winczewski, T. Kallio, M. Vandichel, J. Guerrero-Sánchez, J. G. E. Gardeniers, N. Takeuchi and A. Susarrey-Arce, *Appl Mater Today*, 2022, **28**, 101528.
- 2 Z. L. Wang, J. Choi, M. Xu, X. Hao, H. Zhang, Z. Jiang, M. Zuo, J. Kim, W. Zhou, X. Meng, Q. Yu, Z. Sun, S. Wei, J. Ye, G. G. Wallace, D. L. Officer and Y. Yamauchi, *ChemSusChem*, 2020, **13**, 929–937.
- 3 P. Lu, Y. Yang, J. Yao, M. Wang, S. Dipazir, M. Yuan, J. Zhang, X. Wang, Z. Xie and G. Zhang, *Appl Catal B*, 2019, **241**, 113–119.
- 4 H. Yang, Q. Lin, C. Zhang, X. Yu, Z. Cheng, G. Li, Q. Hu, X. Ren, Q. Zhang, J. Liu and C. He, *Nat Commun*, 2020, **11**, 593.
- 5 C. Han, R. Zhang, Y. Ye, L. Wang, Z. Ma, F. Su, H. Xie, Y. Zhou, P. K. Wong and L. Ye, *J Mater Chem A Mater*, 2019, **7**, 9726–9735.
- 6 S. Nellaippalan and S. Sharma, *ACS Appl Energy Mater*, 2019, **2**, 2998–3003.
- 7 Q. X. Li, D. H. Si, W. Lin, Y. B. Wang, H. J. Zhu, Y. B. Huang and R. Cao, *Sci China Chem*, 2022, **65**, 1584–1593.
- 8 Y. Gang, E. Sarnello, J. Pellessier, S. Fang, M. Suarez, F. Pan, Z. Du, P. Zhang, L. Fang, Y. Liu, T. Li, H. C. Zhou, Y. H. Hu and Y. Li, *ACS Catal*, 2021, **11**, 10333–10344.
- 9 H. Li, K. Gan, R. Li, H. Huang, J. Niu, Z. Chen, J. Zhou, Y. Yu, J. Qiu and X. He, *Adv Funct Mater*, 2023, **33**, 2208622.
- 10 J. Leverett, J. A. Yuwono, P. Kumar, T. Tran-Phu, J. Qu, J. Cairney, X. Wang, A. N. Simonov, R. K. Hocking, B. Johannessen, L. Dai, R. Daiyan and R. Amal, *ACS Energy Lett*, 2022, **7**, 920–928.
- 11 J. Pei, T. Wang, R. Sui, X. Zhang, D. Zhou, F. Qin, X. Zhao, Q. Liu, W. Yan, J. Dong, L. Zheng, A. Li, J. Mao, W. Zhu, W. Chen and Z. Zhuang, *Energy Environ Sci*, 2021, **14**, 3019–3028.
- 12 L. Liao, C. Jia, S. Wu, S. Yu, Z. Wen and S. Ci, *Nanoscale*, 2024, **16**, 8119–8131.
- 13 R. Zhao, Y. Wang, G. Ji, J. Zhong, F. Zhang, M. Chen, S. Tong, P. Wang, Z. Wu, B. Han and Z. Liu, *Advanced Materials*, 2023, **35**, 2205262.
- 14 B. Chen, B. Li, Z. Tian, W. Liu, W. P. Liu, W. Sun, K. Wang, L. Chen and J. Jiang, *Adv Energy Mater*, 2021, **11**, 2102152.
- 15 C. F. Wen, F. Mao, Y. Liu, X. Y. Zhang, H. Q. Fu, L. R. Zheng, P. F. Liu and H. G. Yang, *ACS Catal*, 2020, **10**, 1086–1093.
- 16 J. Chen, X. Wei, R. Cai, J. Ren, M. Ju, X. Lu, X. Long and S. Yang, *ACS Mater Lett*, 2022, **4**, 497–504.
- 17 Z. Ma, T. Zhang, L. Lin, A. Han and J. Liu, *AIChE Journal*, 2023, **69**, e18161.
- 18 D. Sassone, J. Zeng, M. Fontana, M. A. Farkhondehfal, C. F. Pirri and S. Bocchini, *ACS Appl Mater Interfaces*, 2022, **14**, 42144–42152.
- 19 R. Ma, Y. L. Chen, Y. Shen, H. Wang, W. Zhang, S. S. Pang, J. Huang, Y. Han and Y. Zhao, *RSC Adv*, 2020, **10**, 22828–22835.
- 20 Y. Wei, J. Liu, F. Cheng and J. Chen, *J Mater Chem A*, 2019, **7**, 19651–19656.

- 21 J. Jiang, B. Huang, R. Daiyan, B. Subhash, C. Tsounis, Z. Ma, C. Han, Y. Zhao, L. H. Effendi, L. C. Gallington, J. N. Hart, J. A. Scott and N. M. Bedford, *Nano Energy*, 2022, **101**, 107593.
- 22 Y. He, W. J. Jiang, Y. Zhang, L. B. Huang and J. S. Hu, *J Mater Chem A*, 2019, **7**, 18428–18433.
- 23 T. Wang, J. Chen, X. Ren, J. Zhang, J. Ding, Y. Liu, K. H. Lim, J. Wang, X. Li, H. Yang, Y. Huang, S. Kawi and B. Liu, *Angewandte Chemie*, 2023, **62**, e202211174.
- 24 Y. Qian, Y. Liu, H. Tang and B. L. Lin, *J CO₂ Util*, 2020, **42**, 101287.
- 25 Z. Yang, C. Yang, J. Han, W. Zhao, S. Shao, S. Li, H. Gao, H. Xie and X. Zhang, *J Mater Chem A*, 2021, **9**, 19681–19686.
- 26 Z. Li, A. Cao, Q. Zheng, Y. Fu, T. Wang, K. T. Arul, J. L. Chen, B. Yang, N. M. Adli, L. Lei, C. L. Dong, J. Xiao, G. Wu and Y. Hou, *Adv Mater*, 2021, **33**, 2005113.
- 27 B. Ning, M. Liu, Y. Hu, H. Jiang and C. Li, *Dalton Transactions*, 2022, **51**, 3512–3519.
- 28 X. Zhong, T. Yang, S. Liang, Z. Zhong and H. Deng, *Small*, 2023, **19**, 2303185.
- 29 N. Han, Y. Wang, J. Deng, J. Zhou, Y. Wu, H. Yang, P. Ding and Y. Li, *J Mater Chem A*, 2019, **7**, 1267–1272.
- 30 Z. Kuang, W. Zhao, C. Peng, Q. Zhang, Y. Xue, Z. Li, H. Yao, X. Zhou and H. Chen, *ChemSusChem*, 2020, **13**, 5896–5900.
- 31 L. G. Puppin, L. F. da Silva, M. Carmo, H. Varela and O. F. Lopes, *J Mater Res*, 2021, **36**, 4240–4248.
- 32 Z. Chen, T. Fan, Y. Q. Zhang, J. Xiao, M. Gao, N. Duan, J. Zhang, J. Li, Q. Liu, X. Yi and J. L. Luo, *Appl Catal B*, 2020, **261**, 118243.
- 33 G. Liu, Z. Li, J. Shi, K. Sun, Y. Ji, Z. Wang, Y. Qiu, Y. Liu, Z. Wang and P. A. Hu, *Appl Catal B*, 2020, **260**, 118134.
- 34 K. Bejtka, J. Zeng, A. Sacco, M. Castellino, S. Hernández, M. A. Farkhondehfal, U. Savino, S. Ansaloni, C. F. Pirri and A. Chiodoni, *ACS Appl Energy Mater*, 2019, **2**, 3081–3091.
- 35 Z. Wang, W. Tian, J. Zhan, Y. You, L. H. Zhang and F. Yu, *Ind Eng Chem Res*, 2023, **62**, 4940–4946.
- 36 Q. Zhang, Y. Zhang, J. Mao, J. Liu, Y. Zhou, D. Guay and J. Qiao, *ChemSusChem*, 2019, **12**, 1443–1450.
- 37 K. Xu, S. Liu, Z. Cao, Y. Mao and Q. Mao, *Electrochim commun*, 2021, **128**, 107056.
- 38 L. Fan, Z. Xia, M. Xu, Y. Lu and Z. Li, *Adv Funct Mater*, 2018, **28**, 1706289.
- 39 H. Hu, L. Gui, W. Zhou, J. Sun, J. Xu, Q. Wang, B. He and L. Zhao, *Electrochim Acta*, 2018, **285**, 70–77.
- 40 W. Xie, H. Li, G. Cui, J. Li, Y. Song, S. Li, X. Zhang, J. Y. Lee, M. Shao and M. Wei, *Angewandte Chemie*, 2021, **133**, 7458–7464.
- 41 M. S. Amer, H. A. AlOraij and A. M. Al-Mayouf, *J CO₂ Util*, 2024, **82**, 102742.
- 42 A. Hjorth Larsen, J. Jørgen Mortensen, J. Blomqvist, I. E. Castelli, R. Christensen, M. Dułak, J. Friis, M. N. Groves, B. Hammer, C. Hargus, E. D. Hermes, P. C. Jennings, P. Bjerre Jensen, J. Kermode, J. R. Kitchin, E. Leonhard Kolsbjerg, J. Kubal, K. Kaasbjerg, S. Lysgaard, J. Bergmann Maronsson, T. Maxson, T. Olsen, L. Pastewka, A. Peterson, C. Rostgaard, J. Schiøtz, O. Schütt, M. Strange, K. S. Thygesen, T. Vegge, L. Vilhelmsen, M. Walter, Z. Zeng and K. W. Jacobsen, *Journal of Physics: Condensed Matter*, 2017, **29**, 273002.

- 43 N. A. Solopova, N. Dubrovinskaia and L. Dubrovinsky, *Appl Phys Lett*, 2013, **102**, 1–5.
- 44 A. Zakhurdaeva, P. I. Dietrich, H. Hölscher, C. Koos, J. G. Korvink and S. Sharma, *Micromachines (Basel)*, 2017, **8**, 1–10.
- 45 S. K. Jerng, D. S. Yu, J. H. Lee, C. Kim, S. Yoon and S. H. Chun, *Nanoscale Res Lett*, 2011, **6**, 1–6.
- 46 Q. Zhang, H. Zhang and X. L. Cheng, *Chin Physics B*, 2018, **27**, 027301.
- 47 J. Su, Y. Pei, Z. Yang and X. Wang, *RSC Adv*, 2015, **5**, 27229–27234.
- 48 Y. H. Zhao, H. Y. Su, K. Sun, J. Liu and W. X. Li, *Surf Sci*, 2012, **606**, 598–604.
- 49 E. Rugut, D. Joubert and G. Jones, *Comput Mater Sci*, 2021, **187**, 110099.
- 50 L. Braglia, M. Fracchia, P. Ghigna, A. Minguzzi, D. Meroni, R. Edla, M. Vandichel, E. Ahlberg, G. Cerrato and P. Torelli, *J Phys Chem C*, 2020, **124**, 14202–14212.
- 51 M. Calatayud, J. Andrés and A. Beltrán, *Surf Sci*, 1999, **430**, 213–222.
- 52 X. Wang, H. Qin, Y. Chen and J. Hu, *J Phys Chem C*, 2014, **118**, 28548–28561.